

Biowaste-Derived Highly Porous N-Doped Carbon as a Low-Cost Bifunctional Electrocatalyst for Hybrid Sodium–Air Batteries

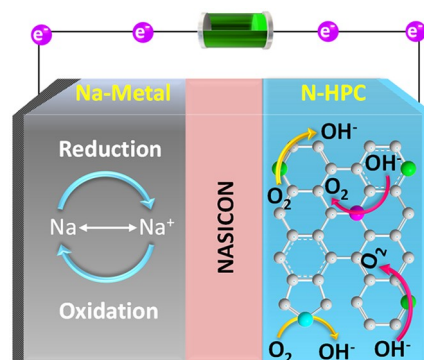
Chinnasamy Murugesan, Baskar Senthilkumar,* and Prabeer Barpanda*

ABSTRACT: Noble-metal-free bifunctional catalysts are vital to improve high-performance, cost-effective metal–air batteries. This work presents highly porous carbon (HPC), derived from waste tree leaves, as a low-cost carbon-based bifunctional electrocatalyst. To further improve the catalytic activity, nitrogen and sulfur doping in HPC is achieved by treating it with urea ($\text{CO}(\text{NH}_2)_2$) and thiourea ($\text{CS}(\text{NH}_2)_2$), respectively. The electrocatalytic oxygen reduction reaction (ORR) and oxygen evolution reaction (OER) activity of the HPC, N-doped HPC, and S-doped HPC have been investigated. Among them, the N-doped HPC was found to show excellent bifunctional electrocatalytic (ORR/OER) activity. The N-doped HPC exhibited a superior bifunctional catalytic activity with an onset potential of 0.95 V (vs RHE) at a current density of 6.31 mA cm^{-2} , whereas in the case of the OER, the observed onset potential was 1.4 V (vs RHE), which is comparable to that of the benchmark RuO_2 (1.45 V vs RHE) catalyst. The assembled hybrid Na–air battery exhibited reversible electrochemical performance with a round-trip efficiency of $\sim 83\%$ over 30 cycles. These economical bifunctional HPC-based catalysts can be effectively employed as air cathodes in hybrid sodium–air battery applications.

KEYWORDS: Biowaste, Highly porous carbon, N/S doping, Bifunctional electrocatalyst, Hybrid Na–air battery

INTRODUCTION

With the rapid increase in global energy demand, various aspects of energy harvesting have become pivotal in the 21st century. Energy from traditional nonrenewable resources leads to increased carbon emission and global warming. The resulting environmental hazards along with possible extinction of nonrenewable (fossil) resources in the near future have led to ever-growing emphasis on sustainable energy generation from inexhaustible renewable sources. In addition, sustainable energy storage is paramount to complement renewable energy generation. Electrochemical energy storage devices are the most viable players in this field for small- to large-scale applications. Ever since their commercialization by Sony in 1991, lithium-ion batteries (LIBs) have become ubiquitous in the modern world thanks to their high energy, power density, and long cycle life.¹ Nonetheless, the growing cost and scarcity of lithium and cobalt resources have restricted their large-scale implementation in grid storage.² In this scenario, metal–air batteries (MABs), having very high capacity, can be harnessed as viable alternatives to metal-ion batteries. Utilizing oxygen as an electron accepting agent,³ these MABs are driven by a series of electrochemical processes including oxygen reduction and oxygen evolution reactions (ORR and OER). The performance of nonaqueous metal–air batteries is grossly affected by clogging arising from insoluble discharge products (e.g., Li_2O_2 , LiO_2).^{3,4} In addition, nonaqueous metal–air batteries also have inadequate reversibility/cyclability. Here, hybrid metal–air



batteries using nonprecious components can be developed as economical alternatives for efficient, high-energy-density energy storage.

From an alkali element point of view, the use of conventional lithium-based chemistry alone cannot meet the diverse applications. Thus, various earth-abundant alkali metals such as Na, K, Zn, Al, and Ca have captured significant attention.⁵ Among these post-Li chemistries, sodium-based batteries are considered as the prime choice due to the abundance, low cost, and undemanding means of extraction and processing of sodium-based resources.⁶ Parallel to the development of Na-ion batteries, the exploration of sodium–air batteries (NABs) has been carried out. NABs offer a high theoretical specific energy of 1683 Wh kg^{-1} , close to that of lithium–air batteries (1700 Wh kg^{-1}).⁷ One major advantage of an aqueous sodium–air battery is the formation of water-soluble discharge products that are reversible. Thus, this increases the cell performance by yielding a high round-trip efficiency, a low overpotential, and good cycling stability.⁸ Despite several merits of aqueous sodium–air batteries, they

warrant the exploration and implementation of efficient bifunctional catalysts with robust ORR and OER activity corresponding to discharge and charge curves, respectively. Most of the reported catalysts are based on precious noble metals that have a high cost and poor durability. Ideal noble-metal catalysts for ORR and OER reactions are Pt/C and IrO₂/RuO₂, respectively, with selective ORR/OER activity.^{9,10} To address these issues, it is necessary to design economical materials demonstrating bifunctional electrocatalytic activity (i.e., having both ORR and OER activity) in an alkaline medium.

In the present work, we have investigated a nontoxic, cost-effective, and environmentally benign green catalyst. Here, graphitic carbon derived from the biodegradable dead ashvattha tree (*Ficus religiosa*) leaves is used as an electrocatalyst for sodium–air batteries. The key reason for choosing the ashvattha tree is its widespread occurrence throughout India, as it has numerous medicinal properties.¹¹ The southern Indian province Tamil Nadu produces a large amount of precious biowaste as dead leaves and fruits every year. Our goal was to utilize these ashvattha leaves as a sustainable source of energy. Unlike other reported synthesis methods involving several steps to produce porous carbon,¹² we have achieved the fabrication of porous carbon with desirable electrochemical performance without using any solvent or template, which is important for environmental benignness and scalability. The merits of eco-friendliness and solvent-/template-free synthesis were utilized to produce graphitic carbon with a high porosity. Subsequently, this graphitic carbon, obtained from waste leaves, is doped with heteroatoms using readily available precursors such as urea and thiourea. The heteroatom-doped graphene (carbon backbone) enhances the catalytically active sites,¹³ exhibiting superior electrocatalytic activity.¹⁴ The heteroatom-doped carbon can be exploited as an electrocatalyst due to the increased catalytic activity and improved active site exposure. This nitrogen-doped highly porous carbon catalyzes ORR activity proportionately to Pt, whereas moderate activity is exhibited for OER reactions. Utilization of a carbon-rich biowaste to make bifunctional electrocatalysts is sustainable and cost-effective. Several studies explored biowastes such as golden shower pod biomass,¹⁵ pomelo peels,¹⁶ soybeans,¹⁷ kidney beans,¹⁸ orange peels,¹⁹ banana peels,²⁰ waste soybean dregs,²¹ aronia, peach stones,²² chicken feather,²³ garlic stems,²⁴ *Acori tatarinowii* rhizoma,²⁵ and Ooty varkey²⁶ and doping with various heteroatoms such as nitrogen (N), sulfur (S), phosphorus (P), and boron (B).^{27–29} Even though these studies have shown potential applications as either bifunctional or trifunctional catalysts, they have seldom been examined for hybrid Na–air battery applications. The present work deals with the synthesis of bifunctional noble-metal-free, highly porous N-doped graphitic carbon derived from biowaste of the ashvattha tree (*Ficus religiosa*) for hybrid Na–air battery applications. The synthesized porous carbon has a specific surface area of 994 m² g⁻¹. The electrocatalytic properties of the carbon-based material were evaluated using linear sweep voltammetry with a rotating ring disk electrode (RRDE). Comparable oxygen evolution activities were achieved for both the Pt/C catalyst and nanostructured N-doped graphitic carbon. Highly porous N-doped graphitic carbon was investigated for the first time as a potential electrocatalyst for a rechargeable hybrid Na–air battery. The resulting hybrid Na–air battery with an N-doped graphitic carbon catalyst as the air cathode yielded a low overpotential

with over 83% round-trip energy efficiency along with stable cycling performance.

EXPERIMENTAL SECTION

Material Synthesis. The highly porous carbon (HPC) product was prepared from dead ashvattha tree (*Ficus religiosa*) leaves by pyrolysis at 400 °C for 5 h followed by carbonization at 600 and 800 °C for 12 h inside a tubular furnace kept under a steady argon flow. Prior to carbonization, the chemical activation was carried out using 1 M KOH as the activating agent. The pyrolyzed carbon was soaked in 1 M KOH overnight, and the sample was filtered and washed several times with deionized water and ethanol. This sample was dried in a vacuum oven at 100 °C for 1 h to remove any residual moisture content. Subsequent N- and S-dopings were performed by treating HPC with urea (CO(NH₂)₂) and thiourea (CS(NH₂)₂), respectively. For N-doping, HPC and urea were blended in a mass ratio of 1:5 and were ground for about 1 h with an agate mortar and pestle. The sample mixture was then calcined at 800 °C for 3 h in a tubular furnace with a steady argon flow. For S-doping, the identical method was used by taking HPC and thiourea.

Characterization. Powder X-ray diffraction (XRD) patterns of as-prepared HPC, calcined at 800 °C, were acquired using a PANalytical X'Pert Pro diffractometer fitted with a Cu K α target of monochromatic wavelength ($\lambda = 1.5404 \text{ \AA}$) operating at 40 kV/30 mA. In the Bragg–Brentano geometry, typical room-temperature diffractograms were obtained in the 2θ range of 10–90° with a scan step of 0.026° s⁻¹. A field emission scanning electron microscope was used to capture the microstructure of the HPC materials (FE-SEM, FEI Inspect F 50 operating at 10 kV). An FEI Tecnai T 20 U-Twin TEM microscope, operating at 200 kV, was used to get high-resolution transmission electron micrographs and selected area diffraction patterns (SAED) of pristine and N-/S-doped HPC. Raman spectra were collected using a LabRAM HR (Horiba Jobin Yvon) unit equipped with a 532 nm (green) laser source. FT-IR spectra of KBr-diluted samples were obtained in the wavenumber window of 400–4000 cm⁻¹ using PerkinElmer (Frontier) equipment.

Preparation and Electrochemical Analyses of Electrocatalysts. For all experiments, a saturated mercury/mercurous oxide (Hg/HgO) electrode was utilized as the reference electrode, the results of which were then converted into the values for a reversible hydrogen electrode (RHE). The electrochemical properties were measured in 0.1 M KOH electrolyte (at 25 °C) using a CH Instruments 7001 E electrochemical workstation with a three-electrode cell configuration consisting of Hg/HgO electrode as the reference electrode, Pt as the counter electrode, and a rotating ring disk electrode (RRDE) loaded with the HPC catalysts as the working electrode. A slurry of the working electrode was drop-casted onto an electrode (4 mm diameter) and dried for more than 30 min under an IR lamp. The scan rate for cyclic voltammetry (CV) and linear sweep voltammetry (LSV) measurements was 10 mV s⁻¹. Chronoamperometry (ORR) tests were performed on all evaluated samples for 36000 s while the voltage was kept constant at -0.3 V (vs the reference electrode Hg/HgO).

Fabrication of Hybrid Sodium–Air Battery. For hybrid Na–air cathode preparation, a slurry was prepared using active materials (N-/S-doped HPC), Super-P carbon black, and polyvinylidene fluoride binder in an 80/10/10 wt % ratio. This slurry was coated onto a circular carbon disk having an area of 0.785 cm². NASICON-type Na₃Zr₂Si₂P₃O₁₂ ceramic pellets (<http://www.4toone.com>) were utilized as solid electrolytes. Pouch-type cells were assembled. The anode compartment in the pouch cell consists of a Na metal anode attached to a nickel mesh and 1 M NaClO₄ in propylene carbonate (PC) solution acting as an organic electrolyte on metallic sodium. The pouch cell was assembled inside the glovebox under high-purity Ar gas. The Ni mesh acts as an anode current collector. This anode part was attached and sealed with the solid electrolyte (Na₃Zr₂Si₂P₃O₁₂) with one side exposed to air as shown in Figure S1 in the Supporting Information. The air cathode, N-doped HPC coated on carbon paper disk, was attached on the air-exposed side of

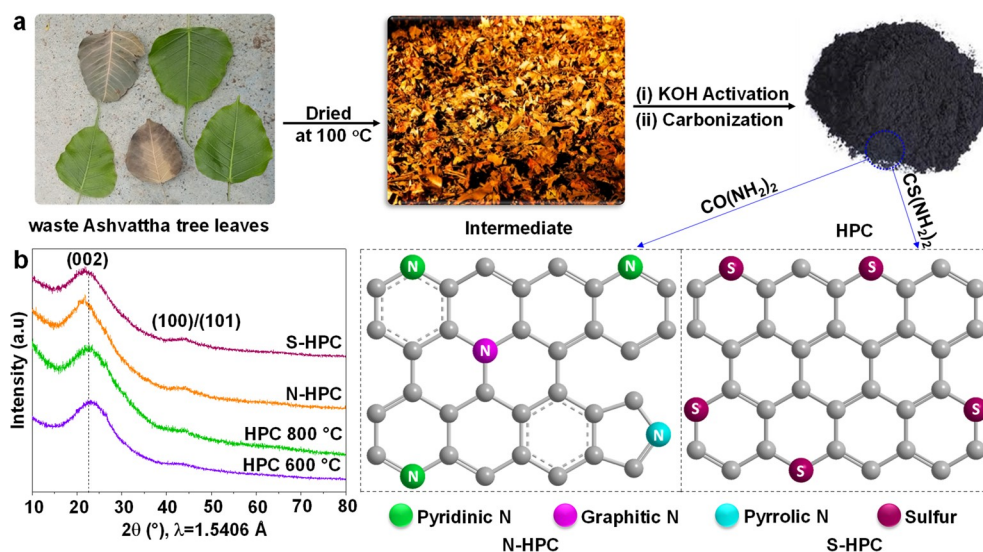


Figure 1. (a) Schematic representation of the synthesis of highly porous carbon and its N/S doping using urea ($\text{CO}(\text{NH}_2)_2$) and thiourea ($\text{CS}(\text{NH}_2)_2$) as N/S sources. (b) X-ray diffraction patterns of HPC, N-HPC, and S-HPC samples showing the two characteristic peaks (002) and (100/101) for the pristine as well as N-/S-doped HPC carbons.

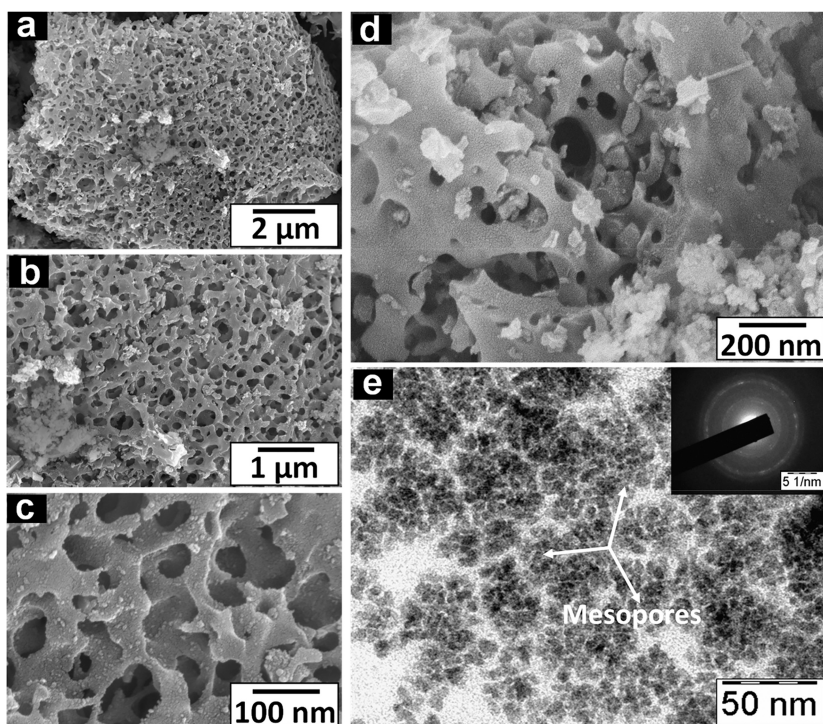


Figure 2. (a–c) Scanning electron microscopy images of HPC showing uniform pores. (d) N-HPC reveals many defects upon N incorporation. (e) Transmission electron microscopy image of HPC revealing the presence of mesopores. Inset: selected area electron diffraction (SAED) pattern confirming the amorphous nature of HPC.

the solid electrolyte. The aqueous electrolyte 0.1 M NaOH was used in the cathode compartment. The final cell configuration can be expressed as $(-)\text{Ni mesh}|\text{metallic Na}|\text{organic electrolyte (1 M NaClO}_4 \cdot \text{PC)}|\text{NASICON (Na}_3\text{Zr}_2\text{Si}_2\text{P}_3\text{O}_{12})|0.1 \text{ M NaOH}|\text{N-doped HPC}|\text{carbon paper}(+)$.

RESULTS AND DISCUSSION

The synthesis of highly porous carbon (HPC) from waste leaves is schematically presented in Figure 1a. The comparative XRD patterns of pristine and N-/S-doped highly porous carbon (N-HPC, S-HPC) are shown in Figure 1b. These

carbon materials feature two broad peaks around 24° and 44° arising from the distinctive carbon (002) and (100/101) planes, respectively. The broad nature of the peaks implied an overall amorphous nature with the local existence of two-dimensional ordering in the carbon matrices together with graphitization.³⁰ Consequently, high-temperature calcination as well as doping agents such as urea and thiourea aid in the production of nanosized grains with a lattice expansion or an increase in interplanar d spacing. It shifted the (002) peak toward a lower 2θ region in case of N- and S-HPC. This hints

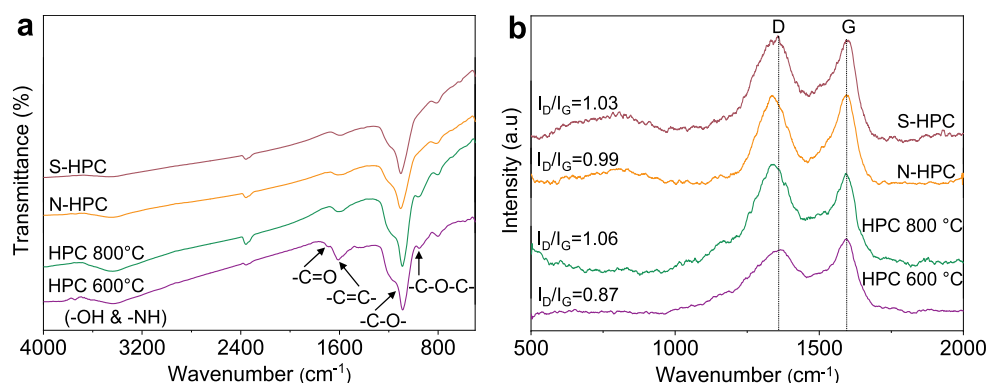


Figure 3. (a) Comparative FTIR spectra revealing the existence of various surface functional groups on HPC carbons. (b) Comparative Raman spectra of HPC-600 °C, HPC-800 °C, N-HPC, and S-HPC samples showing the presence of signature D and G bands.

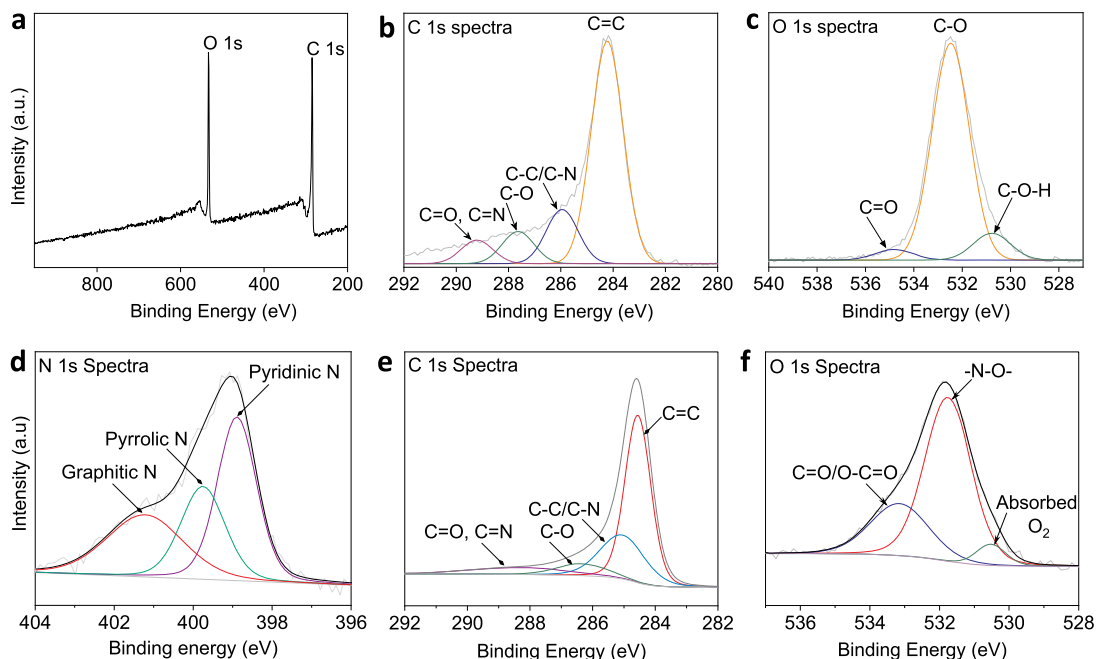


Figure 4. XPS spectra: (a) survey spectrum of HPC showing the existence of carbon and oxygen species; (b, c) corresponding deconvoluted C 1s and O 1s spectra, respectively; (d–f) deconvoluted XPS spectra of N-doped HPC revealing the (d) N 1s, (e) C 1s, and (f) O 1s species present in the HPC samples.

at the nitrogen and sulfur doping of the surface of the highly porous carbon.

Figure 2 illustrates the morphology and porosity of representative pristine and N-HPC material. A porous morphology was clearly observed in the SEM images. Furthermore, several dislocation defects were detected in the graphite layers of the N-HPC, which are created by structural distortion caused by the incorporation of nitrogen atoms into the graphite lattice (Figure 2d). Energy-dispersive X-ray spectra (EDS) of N-doped HPC (Figure S2a,b) proved the successful incorporation N into the carbon matrix. Figure 2e shows a TEM image of uniform-sized mesopores allowing more active sites to be exposed to O₂ adsorption, thereby enhancing the ORR activity. Distinct diffraction rings proved the formation of amorphous carbon.^{31,32}

Various surface functional groups present in the as-prepared HPC and N-/S-doped HPC were analyzed with Fourier transform infrared spectroscopy (FT-IR). These functional groups play an important role in determining the electrocatalytic activity to some extent due to the charge

delocalization of their adjacent carbons. The resulting spectra revealed broad bands at 3350–3380 cm⁻¹ related to the extending vibrations of O–H bonds from hydroxyl absorbed water and carboxylic groups (Figure 3a).³³ The band at 1700 cm⁻¹ can be assigned to the C=O stretching vibrations in carbonyl (C=O) groups.³⁴ The vibrations of aromatic C=C bonds and C=N bonds in the basal plane led to a peak at 1606 cm⁻¹,^{35–37} whereas C–O–C bonds are responsible for a small peak at 951 cm⁻¹. The pronounced broad peak at 950–1260 cm⁻¹ corresponds to the coexistence of carboxyl (O=C–OH), C–O–C (epoxy), and C–OH (hydroxyl) groups.³⁸ For all samples, characteristic D (1350 cm⁻¹) and G (1580 cm⁻¹) Raman bands were captured. The D band stems from in plane imperfections in the graphitic lattice of disordered carbon (e.g., defects and heteroatoms), while the G band arises due to the tangential stretching mode of highly ordered pyrolytic graphite, suggesting the existence of crystalline graphitic carbon. The I_D/I_G ratio was found to increase from 0.87 to 1.06, indicating a high degree of graphitization, which

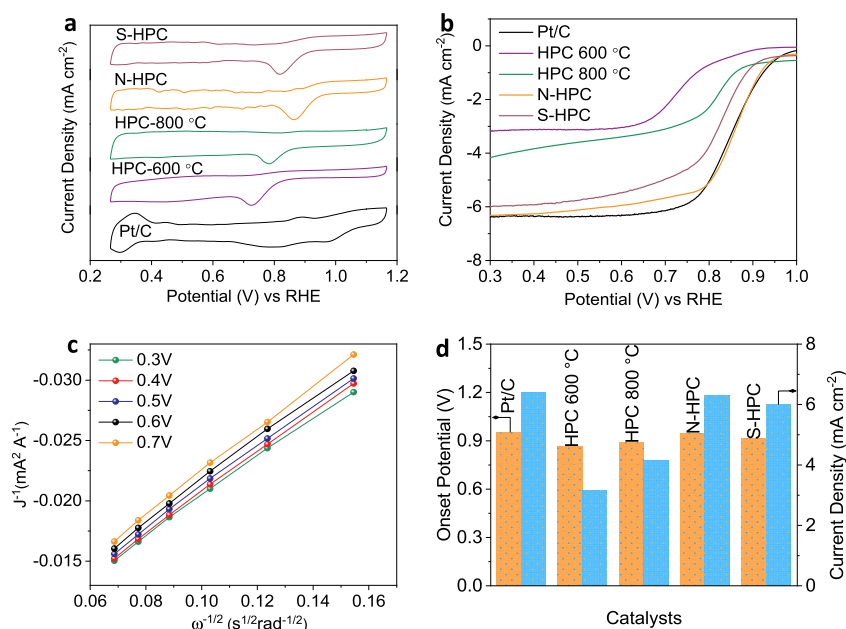


Figure 5. (a) Cyclic voltammograms show the O_2 reduction peaks for all of the tested samples. Among them, N-HPC shows a reduction potential comparable to that of the benchmark Pt/C system. (b) Linear sweep voltammograms (LSVs) plots of HPC-600 °C, HPC-800 °C, N-HPC, and S-HPC carbon samples showing the onset potential values and the exchange current densities (j_0). (c) Koutecky–Levich (K-L) plots of N-HPC recorded at different potentials, validating the four-electron process involved in the ORR process. (d) Comparison of onset potentials and current densities of different carbon catalysts vis-à-vis the reference Pt/C sample.

enhances the electrical conductivity in HPC and N-/S-HPC carbons that in turn enhances the electrocatalytic activity.³⁰

X-ray photoelectron spectroscopy (XPS) was employed to determine the constituent elements and their oxidation states in HPC and N-doped HPC. Figure 4a shows the survey spectrum of pristine HPC with the existence of only carbon and oxygen. The deconvoluted high-resolution C 1s spectrum revealed four individual components, which are C=C, C-C/C-N, C-O and C=O, and C=N at 284.2, 285.9, 287.6, and 289.2 eV, respectively (Figure 4b). The O 1s high-resolution spectrum showed three major peaks at 530.7, 532.5, and 534.8 eV that correspond to C-O-H, C-O, and C=O, respectively (Figure 4c). The N 1s spectrum could be deconvoluted into three kinds of nitrogen species: pyridinic N (398.2 eV), pyrrolic N (399.8 eV), and graphitic N (401.1 eV) (Figure 4d). The constituent atomic percentages in N-HPC have been quantified from an XPS wide spectrum (Figure S3 and Table S1 in the Supporting Information) to be C (88.16%), N (2.23%), and O (9.61%). Previous reports suggested that the pyridinic and graphitic N species can enhance ORR catalytic activity, while the pyrrolic and pyridinic oxides have an insignificant effect on the catalytic activity.^{39–44} The possible reason is that the pyridinic N species could donate one p electron to the aromatic ring in the carbon framework and thus improve the conductivity of the HPC materials. The graphitic N could involve charge delocalization and hence change the chemisorption properties of O_2 molecules.⁴⁵ Different N atoms from pyridinic and graphitic groups perform a crucial role in defining the electrochemical activity of N-doped carbon materials.

Furthermore, the deconvoluted C 1s spectra of N-doped HPC had four different carbon components (Figure 4e). The peaks at 284.6, 285.2, 286.4, and 288.5 eV could be attributed to C=C, C-C/C-N, C-O and C=O, and C=N groups, respectively confirming the successful nitrogen incorporation

into the carbon matrix. Figure 4f depicts the high-resolution O 1s spectra for N-HPC and shows two major peaks at 531.8 and 533.12 eV originating from $-\text{N}-\text{O}-$ and $\text{C}=\text{O}/\text{O}-\text{C}=\text{O}$ oxygen species, respectively. Another minor peak at 530.46 eV might be related to atmospheric oxygen adsorbed by the highly porous carbon.⁴⁶ From the XPS studies, it is evident that various oxygen-containing functional groups are crucial to incorporate N into the carbon framework, which essentially boosts the final electrocatalytic activity.

Subsequently, the electrocatalytic activities of the as-synthesized materials were examined in 0.1 M NaOH electrolyte using a rotating ring disk electrode (RRDE) with a sweep rate of 10 mV s^{-1} . The use of an RRDE rather than an RDE is explained in the Supporting Information. The oxygen reduction activities of all carbon materials were examined using cyclic voltammogram (CV) and linear sweep voltammogram (LSV) techniques. Figure 5a shows the comparative voltammogram profiles of the synthesized materials along with the state of the art Pt/C catalyst. It is obvious from the cyclic voltammogram curves that the redox activity of N-HPC is almost akin to that of the benchmark Pt/C, followed by S-HPC, HPC-800 °C, and HPC-600 °C, as characterized by sharp peaks for N-HPC and S-HPC followed by the other two samples. This redox activity of the doped HPCs could be attributed to the doped and highly porous nature of the materials. The process of doping enables side-on adsorption (Yaegar model), which eventually increases the catalytic activity.⁴⁷ These results emphasize the significant effect of dopants in enhancing the catalytic activity. The superior activity of the doped materials is evident from the linear sweep voltammograms (LSVs) at 1600 rpm with a sweep rate of 10 mVs^{-1} (Figure 5b). The onset potential and current density values were found to be 0.95 V vs RHE and 6.31 mA cm^{-2} for N-HPC and 0.94 V vs RHE and 6 mA cm^{-2} for S-HPC, respectively, which are nearly similar to those of Pt/C (0.1 V vs

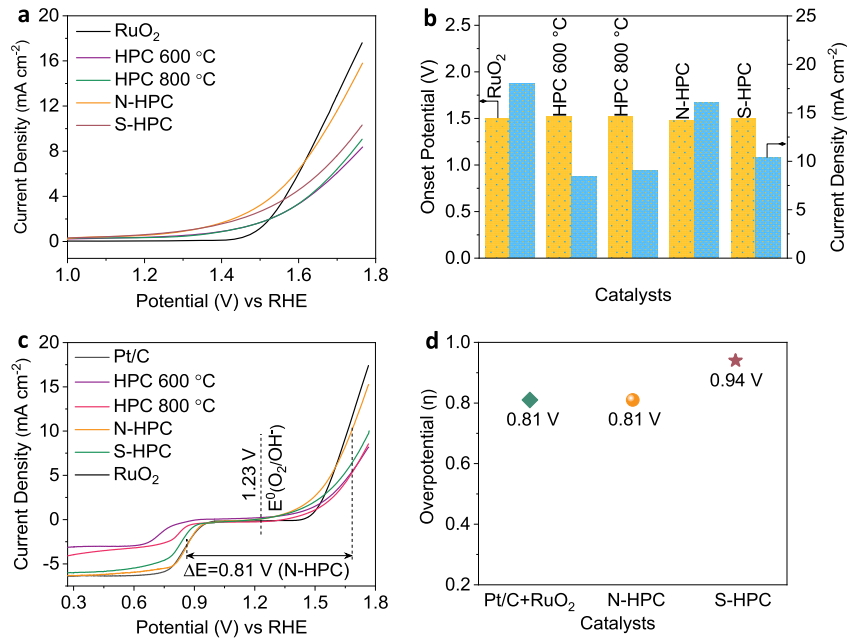


Figure 6. (a) Linear sweep voltammograms of the OER catalysts in 0.1 M NaOH at 10 mV s⁻¹. (b) Comparison of onset potentials and current densities of the catalysts. (c) Overpotential calculation between ORR and OER processes (ΔE ($E_{\text{ORR}} = -3 \text{ mA cm}^{-2} - E_{\text{OER}} = 10 \text{ mA cm}^{-2}$)). (d) Comparison of calculated overpotential values of HPC samples.

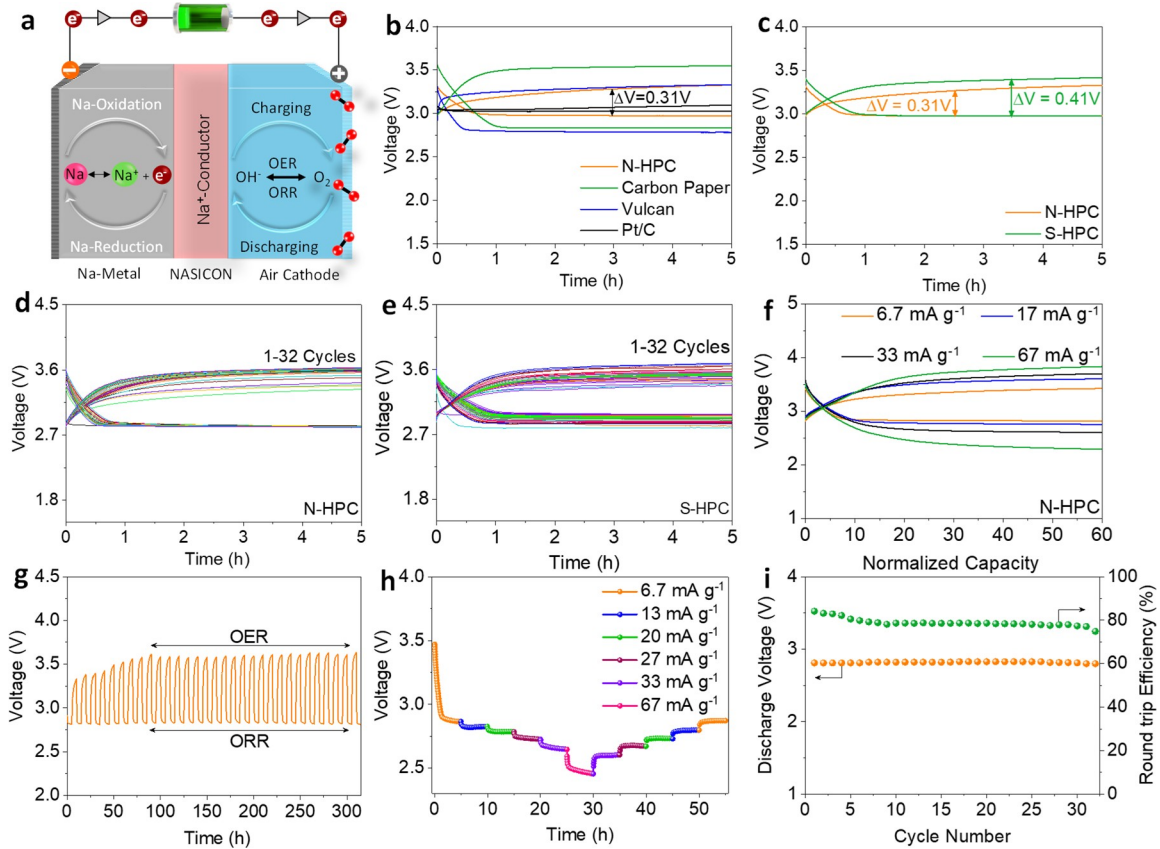


Figure 7. (a) Schematic representation of the hybrid Na-air battery. (b) Comparison of HPC samples as the air cathodes for the Na-air batteries with commercial Pt/C, carbon paper, and Vulcan carbon XC72R, revealing their lower overpotential in comparison with carbon paper and VULCAN carbon XC72R. (c) Comparative air battery performance of N-/S-HPC showing the overpotential difference (ΔE). (d, e) electrochemical performance of N/S-HPC for 32 cycles. (f) Na-air battery performance of N-HPC at different current rates. (g) Electrochemical performance of N-HPC over 300 h showing a stable performance (current density = 6.7 mA g⁻¹). (h) Rate capability of N-HPC at different current densities. (i) Stable discharge voltage and round-trip efficiency of N-HPC for the initial 32 cycles.

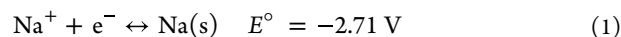
RHE and 6.31 mA cm^{-2} vs RHE). On comparison of the N-HPC and S-HPC, the activity of the N-HPC was found to be close to that of Pt/C in terms of both onset potential and current density. The linear sweep voltammogram profile of N-HPC is given in Figure S4a. The corresponding lower Tafel slope value of N-HPC (93 mV dec^{-1}) in comparison to the Pt/C benchmark (95 mV dec^{-1}) is direct evidence of its superior activity (Figure S4b). Figure 5c displays linear Koutecky–Levich (K-L) plots that convey the first-order dependence of the O_2 kinetics of N-HPC. The histograms of overpotential and current density for various catalysts are given for comparison in Figure 5d. It is evident that the observed values of N-HPC and Pt/C are almost identical in comparison to those of other materials. Further, N-HPC exhibits activity analogous to that of Pt/C in terms of onset and current density. The S-HPC also shows activity closer to that of the benchmark, while the other samples (HPC-800 °C, 0.89 V vs RHE and 4.1 mA cm^{-2} ; HPC-600 °C, 0.9 V vs RHE and 3.1 mA cm^{-2}) deliver activity comparable to that of the Pt/C benchmark. The number of electrons transferred was further calculated for N-HPC and was found to be predominantly a $4e^-$ transfer, which suggests direct conversion of O_2 to OH^- (Figure S5). The catalytic stability was tested for 10 h by an amperometric ($i-t$) technique (Figure S6). N-HPC was found to be highly stable, retaining $\sim 80\%$ of initial activity at the end of 10 h, similarly to the reference Pt/C (77%). This remarkable catalytic activity of N-HPC could be because of the N-doped, highly mesoporous structure with pore diameters ranging from 2 to 25 nm (Figure S7a,b) and the availability of a high surface area for catalytic reactions. The specific BET surface area was found to be $994 \text{ m}^2/\text{g}$, providing a high surface area for adsorption of the incoming species (O_2 in the case of the ORR).⁴⁸ The ORR activity of the N-HPC came from the high surface area and the N-doping on the graphitic lattice contributing the electron donation to the neighboring carbon.

Inspired by the excellent ORR activity of the HPC materials, we investigated their oxygen evolution reactivity in 0.1 M NaOH using an RRDE by sweeping at a rate of 10 mV s^{-1} . Figure 6a presents the comparative LSV plot of the state of the art RuO_2 and those of the HPC samples. N-HPC exhibited activity better than that of RuO_2 in terms of onset potential (N-HPC, 1.4 V vs RHE; RuO_2 , 1.45 V vs RHE) and comparable activity in terms of current density (N-HPC, 16 mA cm^{-2} ; RuO_2 , 18 mA cm^{-2}). The histograms of overpotential and current density values for various catalysts are depicted in Figure 6b. All of the HPC samples have onset potentials superior to that of RuO_2 , but they have relatively poor current density. The bifunctional activities of these HPC carbons along with the state of the art materials are illustrated in Figure 6c,d, showing a superior bifunctional electrocatalytic activity of N-HPC that is comparable to those of the existing benchmark reference systems. Thus, N-HPC is suitable for implementation as an economical bifunctional catalyst in metal–air battery systems.

In this spirit, low-cost HPC-based bifunctional electrocatalysts were exploited as air cathodes for hybrid Na–air batteries. Figure 7a displays a schematic presentation of a rechargeable hybrid (aqueous and aprotic) Na–air battery employing HPC-based electrocatalysts as air cathodes. The hybrid Na–air battery is comprised of Na metal as the anode and a NASICON-type $\text{Na}_3\text{Zr}_2\text{Si}_2\text{P}_3\text{O}_{12}$ solid electrolyte as a selective sodium-ion exchange membrane. The solid electrolyte is also used to separate the cathode and anode parts and

supports Na^+ ions selectively to go through without the mixing of aprotic (1 M NaClO_4 in PC) and aqueous electrolyte (0.1 M NaOH). The final Na–air cell configuration can be expressed as (–)Ni mesh/metallic Nalorganic electrolyte (1 M NaClO_4 : PC)|NASICON ($\text{Na}_3\text{Zr}_2\text{Si}_2\text{P}_3\text{O}_{12}$)| 0.1 M NaOH HPC|carbon paper(+ (Figure S1 in the Supporting Information). During the charging process, an oxygen evolution reaction (OER) occurred in the cathode compartment and Na ions were reduced to Na in the anode compartment. On the other hand, the formation of NaOH followed by an oxygen reduction reaction (ORR) took place in the cathode compartment and Na metal was reduced to Na^+ ions in the anode compartment during the discharge process. These reversible electrochemical reaction processes of fabricated hybrid Na–air cells can be expressed in equations as follows.⁸

At the anode:



At the air cathode:



Overall reaction:



The electrochemical performances of the hybrid sodium–air batteries were examined by galvanostatic charge–discharge measurements. Figure 7b,c shows the resulting charge–discharge curves of the hybrid Na–air batteries with various air cathodes such as Pt/C, carbon paper, Vulcan carbon XC72R, N-doped HPC, and S-doped HPC. ΔV represents the voltage difference between charge and discharge voltages that determines the round-trip efficiency of the batteries. The hybrid Na–air battery with N-doped HPC showed an open circuit voltage (OCV) of $\sim 3.11 \text{ V}$, which reached 3.28 V on constant current charging up to 5 h, while on discharge the cell voltage was observed to be 2.92 V . The ΔV value of N-HPC was estimated to be 0.36 V , which is better than those of S-doped HPC, carbon paper and Vulcan XC 72. In addition, a ΔV comparison plot of N-/S-HPC with the benchmarks Pt/C and Ir/C is provided in Figure S8 in the Supporting Information. Among all samples, the best ORR catalyst Pt/C registered the lowest overpotential of 0.15 V , whereas N-HPC exhibited an overpotential value of 0.31 V , which is relatively lower than those of both S-HPC and Ir/C. The round-trip efficiency of the cell was calculated to be $\sim 83\%$ at a current density of 0.01 mA cm^{-2} , which is greater than those of nonaqueous sodium–air batteries. The N-HPC catalyst exhibited excellent rechargeability and improved performance among all of the catalysts.

Further, cycling stabilities of the N-doped and S-doped HPC Na–air batteries were studied up to 30 cycles, as shown in Figure 7d,e. The ΔV value increased in the initial cycles and was stabilized in prolonged cycles. Further, the rate capability, power density, and cycling stability of the best-performing Na–air batteries comprising N-doped HPC were investigated (Figure 7f–i). An Na–air battery with N-doped HPC as the cathode exhibited a maximum power density of $\sim 160 \text{ mW g}^{-1}$ at a current density of 70 mA g^{-1} . This outstanding performance of the N-doped HPC based Na–air cells relative to other Na–air cells could be due to (i) an excellent bifunctional activity, (ii) an enhanced electronic conductivity, and (iii) a high surface area due to the mesoporous structure of

N-doped HPC. The electrochemical properties of N-HPC carbon have been compared to all reported materials (given in Table S2), showing its superior performance. Though numerous biowaste-derived carbon materials have been investigated as potential bifunctional electrocatalysts, their implementation in hybrid air batteries has not been explored. These eco-friendly catalysts can be exploited as air cathodes in hybrid Na–air batteries for future energy storage technologies.

CONCLUSIONS

Biowaste-derived highly porous carbon and its derivatives were prepared by chemical activation followed by pyrolysis using a 1 M KOH agent. Subsequently, N/S doping into this carbon was conducted by treating samples with urea and thiourea. The resulting highly porous carbon and its derivatives exhibited excellent bifunctional electrocatalytic activity. Among them, a superior performance was observed for nitrogen-doped carbon (N-HPC). This promising bifunctional activity of N-HPC originated from electron donation from the nitrogen dopant to the graphitic lattice along with the high surface area (994 m²/g), facilitating the exposure of more active sites. Moreover, the unique micro-/mesoporous morphology and the high surface area to volume ratio in this system can lead to a higher density of active catalytic sites that enable fast transport of reactants, ions, and electrons. The presence of N-doped graphitic domains and the high degree of graphitization can contribute to the catalytic activity of the catalyst. When it is implemented as an air cathode in a hybrid Na–air battery, the N-doped HPC showed stable/reversible (dis)charge activity with a round-trip efficiency of ~83% at a current density of 0.01 mA cm⁻², which is higher than those of currently available nonaqueous lithium–air batteries. Biowaste-prepared carbons can act as economic bifunctional catalysts for hybrid sodium–air batteries.

AUTHOR INFORMATION

Corresponding Authors

Baskar Senthilkumar – Faraday Materials Laboratory (FaMaL), Materials Research Center, Indian Institute of Science, Bangalore 560012, India; Amrita Centre for Nanosciences and Molecular Medicine, Amrita Vishwa Vidyapeetham, Kochi 682041, India; Email: senthilkumarb@acnsmm.aims.amrita.edu

Prabeer Barpanda – Faraday Materials Laboratory (FaMaL), Materials Research Center, Indian Institute of Science, Bangalore 560012, India; Helmholtz Institute Ulm (HIU), Ulm 89081, Germany; orcid.org/0000-0003-0902-3690; Email: prabeer@iisc.ac.in

Author

Chinnasamy Murugesan – Faraday Materials Laboratory (FaMaL), Materials Research Center, Indian Institute of Science, Bangalore 560012, India; School of Chemistry, University of St. Andrews, St. Andrews, Fife KY16 9ST, Scotland, U.K.

Author Contributions

C.M.: investigation, methodology, data curation, writing-original draft. B.S.: validation, conceptualization, formal analysis, investigation, writing-original draft. P.B.: supervision, funding acquisition, project administration, writing-reviewing and editing.

Notes

The authors declare no competing financial interest.

ACKNOWLEDGMENTS

The authors gratefully acknowledge the financial support from the Technology Mission Division (Department of Science & Technology, Government of India) under the aegis of the Materials for Energy Storage (MES-2018) program (DST/TMD/MES/2k18/00217). B.S. thanks the DST for providing a National Postdoctoral Fellowship (PDF/2015/00217). P.B. is grateful to the Alexander von Humboldt Foundation (Bonn, Germany) for a 2022 Humboldt fellowship for experienced researchers. P.B. thanks Prof. Dr. Max Fichtner for hosting him at HIU, Ulm, Germany. We thank S. T. Senthilkumar and S. P. Panjalingam for their technical help and discussions.

REFERENCES

- (1) Lee, D. U.; Fu, J.; Park, M. G.; Liu, H.; Kashkooli, A. G.; Chen, Z. Self-assembled NiO/Ni(OH)₂ nanoflakes as active material for high-power and high-energy hybrid rechargeable battery. *Nano Lett.* **2016**, *16* (3), 1794–1802.
- (2) Khan, Z.; Senthilkumar, B.; Park, S. O.; Park, S.; Yang, J.; Lee, J. H.; Song, H.-K.; Kim, Y.; Kwak, S. K.; Ko, H. Carambola-shaped VO₂ nanostructures: a binder-free air electrode for an aqueous Na–air battery. *J. Mater. Chem. A* **2017**, *5* (5), 2037–2044.
- (3) Shin, D.; Jeong, B.; Choun, M.; Ocon, J. D.; Lee, J. Diagnosis of the measurement inconsistencies of carbon-based electrocatalysts for the oxygen reduction reaction in alkaline media. *RSC Adv.* **2015**, *5* (2), 1571–1580.
- (4) Cheon, J. Y.; Kim, K.; Sa, Y. J.; Sahgong, S. H.; Hong, Y.; Woo, J.; Yim, S.-D.; Jeong, H. Y.; Kim, Y.; Joo, S. H. Graphitic nanoshell/mesoporous carbon nanohybrids as highly efficient and stable bifunctional oxygen electrocatalysts for rechargeable aqueous Na–air batteries. *Adv. Energy Mater.* **2016**, *6* (7), 1501794.
- (5) Kwak, W.-J.; Chen, Z.; Yoon, C. S.; Lee, J.-K.; Amine, K.; Sun, Y.-K. Nanoconfinement of low-conductivity products in rechargeable sodium–air batteries. *Nano Energy* **2015**, *12*, 123–130.
- (6) Das, S. K.; Lau, S.; Archer, L. A. Sodium–oxygen batteries: a new class of metal–air batteries. *J. Mater. Chem. A* **2014**, *2* (32), 12623–12629.
- (7) Girishkumar, G.; McCloskey, B.; Luntz, A. C.; Swanson, S.; Wilcke, W. Lithium–air battery: promise and challenges. *J. Phys. Chem. Lett.* **2010**, *1* (14), 2193–2203.
- (8) Senthilkumar, B.; Khan, Z.; Park, S.; Seo, I.; Ko, H.; Kim, Y. Exploration of cobalt phosphate as a potential catalyst for rechargeable aqueous sodium-air battery. *J. Power Sources* **2016**, *311*, 29–34.
- (9) Zhao, Y.; Kamiya, K.; Hashimoto, K.; Nakanishi, S. Efficient bifunctional Fe/C/N electrocatalysts for oxygen reduction and evolution reaction. *J. Phys. Chem. C* **2015**, *119* (5), 2583–2588.

- (10) Tian, G. L.; Zhao, M. Q.; Yu, D.; Kong, X. Y.; Huang, J. Q.; Zhang, Q.; Wei, F. Nitrogen-doped graphene/carbon nanotube hybrids: in situ formation on bifunctional catalysts and their superior electrocatalytic activity for oxygen evolution/reduction reaction. *Small* **2014**, *10* (11), 2251–9.
- (11) Gautam, S.; Meshram, A.; Bhagyawant, S. S.; Srivastava, N. Ficus religiosa-potential role in pharmaceuticals. *Int. J. Pharm. Sci. Res.* **2014**, *5* (5), 1616–1623.
- (12) Chen, P.; Wang, L.-K.; Wang, G.; Gao, M.-R.; Ge, J.; Yuan, W.-J.; Shen, Y.-H.; Xie, A.-J.; Yu, S.-H. Nitrogen-doped nanoporous carbon nanosheets derived from plant biomass: an efficient catalyst for oxygen reduction reaction. *Energy Environ. Sci.* **2014**, *7* (12), 4095–4103.
- (13) Park, H. W.; Lee, D. U.; Nazar, L. F.; Chen, Z. Oxygen reduction reaction using MnO₂ nanotubes/nitrogen-doped exfoliated graphene hybrid catalyst for Li-O₂ battery applications. *J. Electrochem. Soc.* **2013**, *160* (2), A344–A350.
- (14) Park, H. W.; Lee, D. U.; Liu, Y.; Wu, J.; Nazar, L. F.; Chen, Z. Bi-functional N-doped CNT/graphene composite as highly active and durable electrocatalyst for metal air battery applications. *J. Electrochem. Soc.* **2013**, *160* (11), A2244–A2250.
- (15) Sathiskumar, C.; Ramakrishnan, S.; Vinothkannan, M.; Rhan, K. A.; Karthikeyan, S.; Yoo, D. J. Nitrogen-doped porous carbon derived from biomass used as trifunctional electrocatalyst toward oxygen reduction, oxygen evolution and hydrogen evolution reactions. *Nanomaterials* **2020**, *10* (1), 76.
- (16) Wang, Y.; Zhu, M.; Wang, G.; Dai, B.; Yu, F.; Tian, Z.; Guo, X. Enhanced oxygen reduction reaction by in situ anchoring Fe₂N nanoparticles on nitrogen-doped pomelo peel-derived carbon. *Nanomaterials* **2017**, *7* (11), 404.
- (17) Guo, C.-Z.; Liao, W.-L.; Chen, C.-G. Design of a non-precious metal electrocatalyst for alkaline electrolyte oxygen reduction by using soybean biomass as the nitrogen source of electrocatalytically active center structures. *J. Power Sources* **2014**, *269*, 841–847.
- (18) Ma, X.; Feng, S.; Ji, S. Nitrogen-doped carbon with hierarchical porous structure for electrocatalysis of oxygen reduction reaction. *Int. J. Electrochem. Sci.* **2017**, *12*, 7869–7876.
- (19) Dhelipan, M.; Arunchander, A.; Sahu, A. K.; Kalpana, D. Activated carbon from orange peels as supercapacitor electrode and catalyst support for oxygen reduction reaction in proton exchange membrane fuel cell. *J. Saudi Chem. Soc.* **2017**, *21* (4), 487–494.
- (20) Pérez-Rodríguez, S.; Sebastián, D.; Alegre, C.; Tsoncheva, T.; Petrov, N.; Paneva, D.; Lázaro, M. J. Biomass waste-derived nitrogen and iron co-doped nanoporous carbons as electrocatalysts for the oxygen reduction reaction. *Electrochim. Acta* **2021**, *387*, 138490.
- (21) Tyagi, A.; Banerjee, S.; Singh, S.; Kar, K. K. Biowaste derived activated carbon electrocatalyst for oxygen reduction reaction: effect of chemical activation. *Int. J. Hydrog. Energy* **2020**, *45* (34), 16930–16943.
- (22) Ma, Z.; Wang, K.; Qiu, Y.; Liu, X.; Cao, C.; Feng, Y.; Hu, P. Nitrogen and sulfur co-doped porous carbon derived from bio-waste as a promising electrocatalyst for zinc-air battery. *Energy* **2018**, *143*, 43–55.
- (23) Li, Q.; He, T.; Zhang, Y.-Q.; Wu, H.; Liu, J.; Qi, Y.; Lei, Y.; Chen, H.; Sun, Z.; Peng, C.; Yi, L.; Zhang, Y. Biomass waste-derived 3D metal-free porous carbon as a bifunctional electrocatalyst for rechargeable zinc–air batteries. *ACS Sustainable Chem. Eng.* **2019**, *7* (20), 17039–17046.
- (24) Prabu, N.; Kesavan, T.; Maduraiveeran, G.; Sasidharan, M. Bio-derived nanoporous activated carbon sheets as electrocatalyst for enhanced electrochemical water splitting. *Int. J. Hydrog. Energy* **2019**, *44* (36), 19995–20006.
- (25) Wang, Y.; Zhu, M.; Li, Y.; Zhang, M.; Xue, X.; Shi, Y.; Dai, B.; Guo, X.; Yu, F. Heteroatom-doped porous carbon from methyl orange dye wastewater for oxygen reduction. *Green Energy Environ.* **2018**, *3* (2), 172–178.
- (26) Chen, Y.; Wang, H.; Ji, S.; Lv, W.; Wang, R. Harvesting a 3D N-doped carbon network from waste bean dregs by ionothermal carbonization as an electrocatalyst for an oxygen reduction reaction. *Materials* **2017**, *10* (12), 1366.
- (27) Li, Z.; Gao, Q.; Qian, W.; Tian, W.; Zhang, H.; Zhang, Q.; Liu, Z. Ultrahigh oxygen reduction reaction electrocatalytic activity and stability over hierarchical nanoporous N-doped carbon. *Sci. Rep.* **2018**, *8* (1), 2863.
- (28) Hu, C.; Yi, Z.; She, W.; Wang, J.; Xiao, J.; Wang, S. Urchin-like non-precious-metal bifunctional oxygen electrocatalysts: Boosting the catalytic activity via the In-situ growth of heteroatom (N, S)-doped carbon nanotube on mesoporous cobalt sulfide/carbon spheres. *J. Colloid Interface Sci.* **2018**, *524*, 465–474.
- (29) Yang, X.; Li, K.; Cheng, D.; Pang, W.-L.; Lv, J.; Chen, X.; Zang, H.-Y.; Wu, X.-L.; Tan, H.-Q.; Wang, Y.-H.; Li, Y.-G. Nitrogen-doped porous carbon: highly efficient trifunctional electrocatalyst for oxygen reversible catalysis and nitrogen reduction reaction. *J. Mater. Chem. A* **2018**, *6* (17), 7762–7769.
- (30) Zhang, L.; Su, Z.; Jiang, F.; Yang, L.; Qian, J.; Zhou, Y.; Li, W.; Hong, M. Highly graphitized nitrogen-doped porous carbon nanopolyhedra derived from ZIF-8 nanocrystals as efficient electrocatalysts for oxygen reduction reactions. *Nanoscale* **2014**, *6* (12), 6590–6602.
- (31) He, W.; Jiang, C.; Wang, J.; Lu, L. High-rate oxygen electroreduction over graphitic-N species exposed on 3D hierarchically porous nitrogen-doped carbons. *Angew. Chem., Int. Ed.* **2014**, *53* (36), 9503–9507.
- (32) Zhang, P.; Sun, F.; Xiang, Z.; Shen, Z.; Yun, J.; Cao, D. ZIF-derived in situ nitrogen-doped porous carbons as efficient metal-free electrocatalysts for oxygen reduction reaction. *Energy Environ. Sci.* **2014**, *7* (1), 442–450.
- (33) Guo, D.; Xin, R.; Zhang, Z.; Jiang, W.; Hu, G.; Fan, M. N-doped hierarchically micro- and mesoporous carbons with superior performance in supercapacitors. *Electrochim. Acta* **2018**, *291*, 103–113.
- (34) Pan, N.; Guan, D.; Yang, Y.; Huang, Z.; Wang, R.; Jin, Y.; Xia, C. A rapid low-temperature synthetic method leading to large-scale carboxyl graphene. *Chem. Eng. J.* **2014**, *236*, 471–479.
- (35) Shlyakhova, E. V.; Bulusheva, L. G.; Kanygin, M. A.; Plyusnin, P. E.; Kovalenko, K. A.; Senkovskiy, B. V.; Okotrub, A. V. Synthesis of nitrogen-containing porous carbon using calcium oxide nanoparticles. *Phys. Status Solid B* **2014**, *251* (12), 2607–2612.
- (36) AlQadhi, N. F.; AlSuhaimi, A. O. Chemically functionalized activated carbon with 8-hydroxyquinoline using aryldiazonium salts/diazotization route: Green chemistry synthesis for oxins-carbon chelators. *Arab. J. Chem.* **2020**, *13* (1), 1386–1396.
- (37) Geng, D.; Yang, S.; Zhang, Y.; Yang, J.; Liu, J.; Li, R.; Sham, T.-K.; Sun, X.; Ye, S.; Knights, S. Nitrogen doping effects on the structure of graphene. *Appl. Surf. Sci.* **2011**, *257* (21), 9193–9198.
- (38) Kumar, M. P.; Kesavan, T.; Kalita, G.; Ragupathy, P.; Narayanan, T. N.; Pattanayak, D. K. On the large capacitance of nitrogen doped graphene derived by a facile route. *RSC Adv.* **2014**, *4* (73), 38689–38697.
- (39) Oh, H.-S.; Kim, H. The role of transition metals in non-precious nitrogen-modified carbon-based electrocatalysts for oxygen reduction reaction. *J. Power Sources* **2012**, *212*, 220–225.
- (40) Xiang, Z.; Xue, Y.; Cao, D.; Huang, L.; Chen, J.-F.; Dai, L. Highly efficient electrocatalysts for oxygen reduction based on 2D covalent organic polymers complexed with non-precious metals. *Angew. Chem., Int. Ed.* **2014**, *53* (9), 2433–2437.
- (41) Wang, Z.; Li, B.; Ge, X.; Goh, F. W. T.; Zhang, X.; Du, G.; Wu, D.; Liu, Z.; Andy Hor, T. S.; Zhang, H.; Zong, Y. Co@Co₃O₄@PPD core@biregular nanoparticle-based composite as an efficient electrocatalyst for oxygen reduction reaction. *Small* **2016**, *12* (19), 2580–2587.
- (42) Deng, D.; Yu, L.; Chen, X.; Wang, G.; Jin, L.; Pan, X.; Deng, J.; Sun, G.; Bao, X. Iron encapsulated within pod-like carbon nanotubes for oxygen reduction reaction. *Angew. Chem., Int. Ed.* **2013**, *52* (1), 371–375.
- (43) Liang, Y.; Li, Y.; Wang, H.; Zhou, J.; Wang, J.; Regier, T.; Dai, H. Co₃O₄ nanocrystals on graphene as a synergistic catalyst for oxygen reduction reaction. *Nat. Mater.* **2011**, *10* (10), 780–786.

(44) Wu, G.; More, K. L.; Johnston, C. M.; Zelenay, P. High-performance electrocatalysts for oxygen reduction derived from polyaniline, iron, and cobalt. *Science* **2011**, 332 (6028), 443–447.

(45) Gong, K.; Du, F.; Xia, Z.; Durstock, M.; Dai, L. Nitrogen-doped carbon nanotube arrays with high electrocatalytic activity for oxygen reduction. *Science* **2009**, 323 (5915), 760–764.

(46) Collins, P. G.; Bradley, K.; Ishigami, M.; Zettl, A. Extreme oxygen sensitivity of electronic properties of carbon nanotubes. *Science* **2000**, 287 (5459), 1801–1804.

(47) Dunn, B.; Kamath, H.; Tarascon, J. M. Electrical energy storage for the grid: a battery of choices. *Science* **2011**, 334 (6058), 928–35.

(48) Zhang, J.; Zhao, Z.; Xia, Z.; Dai, L. A metal-free bifunctional electrocatalyst for oxygen reduction and oxygen evolution reactions. *Nat. Nanotechnol.* **2015**, 10 (5), 444–452.